Journal of Materials Chemistry A

Extended Layer-by-Layer Madelung Potential Analysis on Layered Oxyhalides Photocatalysts and Other Layered Systems

Journal:	*Journal of Materials Chemistry A*
Manuscript ID	TA-ART-05-2019-005201.R1
Article Type:	Paper
Date Submitted by the Author:	18-Jul-2019
Complete List of Authors:	Kato, Daichi; Kyoto University, Graduate School of Engineeing Abe, Ryu; Kyoto University, Graduate School of Engineeing Kageyama, Hiroshi; Kyoto University, Department of Energy and Hydrocarbon Chemistry

ARTICLE

Extended Layer-by-Layer Madelung Potential Analysis on Layered Oxyhalides Photocatalysts and Other Layered Systems†

Received 00th January 20xx,
Accepted 00th January 20xx

DOI: 10.1039/x0xx00000x

Daichi Kato,[a] *Ryu Abe,*[*,a,b] *and Hiroshi Kageyama*[*,a,b]

A recent study on Bi_4NbO_8Cl and related Bi-based layered oxyhalide photocatalysts using a layer-by-layer Madelung potential (L^2MP) analysis with a sphere model revealed that oxide anions in the fluorite-type slab of Bi_4NbO_8Cl are electrostatically destabilized by 2nd nearest sublayer composed of the apical oxygen of the perovskite slab. Here we provide an extended L^2MP analysis for the Bi-based layered oxyhalides using a modified (square-prism) model and apply it to other layered compounds. It is found that consideration of up to 3rd nearest sublayer is necessary to account for the nearly equal valence band maximum between Bi_2GdO_4X and Bi_4NbO_8Cl. Additionally, BiOX and Bi_2GdO_4X show a distinct X-dependence of the Madelung site potential of oxide anions. The L^2MP analysis on Bi_2WO_6, $Sr_3Sc_2Cu_2S_2O_5$ and $Sr_2ScCuSO_3$ revealed a sizable contribution of distant layers to their electrostatic potentials. This study demonstrates that this method can be applicable to a wide range of layered materials and serves as a powerful guide toward finding composition and layer stacking sequence suitable for photocatalysis and other functions.

Introduction

There is an intimate relationship between the crystal structures of extended solids and the properties they exhibit. One of the key descriptors for ionic solids is the Madelung site potential, or the sum of the electrostatic potentials created at specific crystallographic site from surrounding ions. The Madelung site potential was used to explain band formation of ionic solids such as NaCl, ZnS and $SrTiO_3$ in 1960-70's,[1-3] and high-T_c cuprate superconductors in 1980-90's.[4-6] In recent years, there is a renewed interest in using Madelung site potential, for example, valence skip fluctuation in $BaBiO_3$,[7] the surface defect behaviour of metal oxide,[8] and the band location in eight TiO_2 polymorphs.[9, 10] Despite the long-range nature of Coulomb interaction, however, the difference in Madelung site potential is mainly explained by the local coordination environment and less attention appears to be paid to distant ions.[4, 9, 10]

Recently, we have developed a series of layered bismuth oxyhalides photocatalysts, Bi_4NbO_8Cl[11] and its derivatives,[12-14] as highly efficient visible-light responsive photocatalysts for water splitting with extraordinary stability against self-oxidative deactivation by photo-generated holes. The photocatalytic stability in Bi_4NbO_8Cl and its narrow band gap (2.39 eV) are attributed to the occupation of O 2p orbitals at the valence band maximum (VBM) rather than Cl 3p orbitals. The unusual upward shift of oxygen 2p bands is understood in terms of Madelung site potential of anions[15] as well as Bi lone pair effect.[16] In particular, Madelung site potential calculation revealed that the oxide anion in the fluorite-type blocks of Bi_4NbO_8X (X = Cl, Br) (Figure 1b) and Bi_2GdO_4X (Figure 1c) has a lower Madelung site potential in comparison with BiOX (Figure 1a), leading to the upward shift of VBM. To further clarify the role and contribution of each layer, we subsequently developed a layer-by-layer Madelung potential (L^2MP) analysis and found that the destabilization of the oxide anion in Bi_4NbO_8X and Bi_2GdO_4X is due to strong repulsive interactions from the oxide anions in the 2nd nearest-neighbor sublayer (2NNL; Figure 1),[15] as shown in Figure 2 (left) and Figure S3.

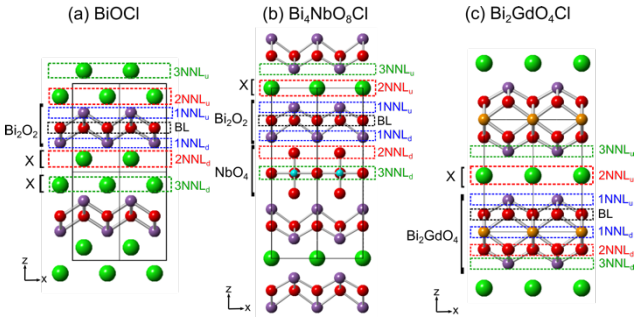

Figure 1. Crystal structures of (a) BiOX (X = Cl, Br, I), (b) Bi_4NbO_8X (X = Cl, Br) and (c) Bi_2GdO_4X (X = Cl, Br, I). The fluorite-derived basal layer (BL) and its neighboring sublayers (*n*-th nearest-neighbor layer; *n*NNL) are indicated. Purple, red, yellow-green and blue spheres, respectively, represent Bi, O, halogen (X) and Nb atoms. The non-distorted structure is given for (b). For each, the unit cell is indicated by solid black lines.

[a] *Department of Energy and Hydrocarbon Chemistry, Graduate School of Engineering, Kyoto University, Nishikyo-ku, Kyoto 615-8510, Japan*
[b] *CREST, Japan Science and Technology Agency (JST), Kawaguchi, Saitama 332-0012, Japan*

† Electronic Supplementary Information (ESI) available: Detailed discussion on electrostatic potential from surrounding sub-layers in BiOCl and crystal structures and the value of Madelung site potential, *etc*. (PDF). See DOI: 10.1039/x0xx00000x

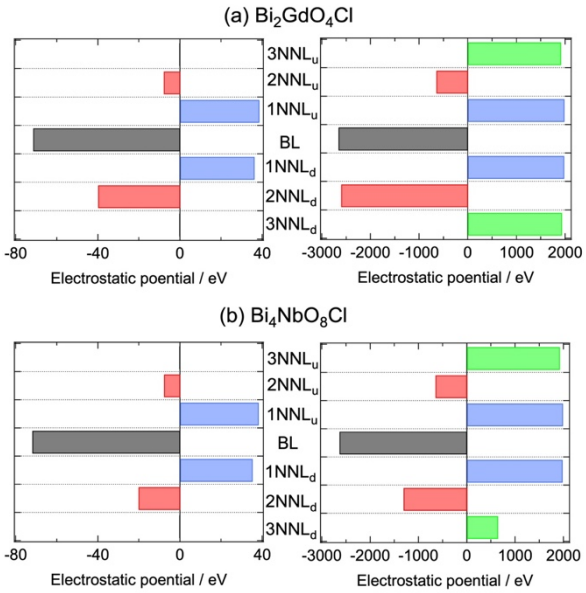

Figure 2. Electrostatic potential at the oxygen site in the fluorite-type layer from adjacent sublayers. Calculation using (left) the sphere model[15] and (right) the square-prism model (this work) for A = 200 Å (Figure 3). The non-distorted hypothetical structure was used for Bi_4NbO_8Cl.

Given the long-range nature of Coulomb interactions, further sublayers may also affect the valence band structures of these Bi-based oxyhalides. However, the sphere model (Figure 3a), where the electrostatic potentials of ions within R = 4 Å from the oxide anion in the fluorite-type layers were taken into consideration, cannot properly extract the contribution of the distant sublayers such as 3NNL.[15] In addition, the effect of halogen (X) on their Madelung potential has not been addressed, in spite of the fact that isostructural (Cl, Br, I) oxyhalides have different band gaps. More importantly, the aforementioned compounds are just a few examples of more than 100 oxyhalides with the Bi_2O_2 fluorite layer.[17] Furthermore, there are a number of modular compounds whose structures are built from slabs of a parent motif interleaved with other layers. Available building blocks include anti-fluorite, rock-salt and perovskite layers to name only a few. Such structural diversity in layered materials has resulted in a wide range of functional properties including superconductivity in cupurates,[18] FeAs- and BiS_2-based compounds,[19-21] secondary battery in layered rock-salt oxides,[22] transparent conductivity in Cu_2S_2-based compounds[23, 24]. We thus expect that Madelung analysis could be applied to other layered systems toward obtaining desired photocatalytic activities and other functions.

This study aims to address these issues by including a wider range of ions for BiOX, Bi_4NbO_8X and Bi_2GdO_4X as well as other classes of layered materials. Two alternate models are employed for layer-by-layer Madelung potential (L^2MP) analysis by changing the size included in the calculation. This extended analysis revealed that a 3NN sublayer plays a crucial role in the valence band structures in Bi_2GdO_4X and Bi_4NbO_8Cl, while the origin of X-dependence of the band gap is discussed. In addition, L^2MP analysis is also applied to Bi_2WO_6, $Sr_3Sc_2Cu_2S_2O_5$ and $Sr_2ScCuSO_3$ to investigate the impact of distant sublayer on their Madelung potential.

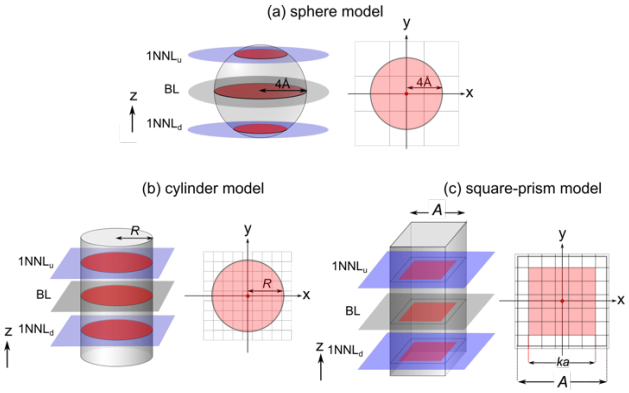

Figure 3. Three models employed for calculating electrostatic potential at the oxygen site in BL from each sublayer: (a) sphere model,[15] (b) cylinder model, and (c) square-prism model. For each model, cations and anions within the red area are taken into considerations. On the right side of each panel, the unit cell is indicated in grey. The red area for the square-prism model shows $-ka/2 \le x, y \le ka/2$ (where k is an odd number satisfying $ka \le A \le (k+1)a$). The oxide anion in question is placed at the center of (a) sphere, (b) circle, and (c) square.

Methods

Electrostatic potential was calculated using structural data reported in Refs. 25-31. For Bi_4NbO_8Cl and Bi_2WO_6, non-distorted lattices were constructed, where the atomic coordinates of each atomic position were set to the average values of experimentally obtained structures, as shown in Table S1 and Table S2.[25, 31] Structural optimization based on density functional theory (DFT) was performed for the hypothetical Bi_4NbO_8Cl structure using the Cambridge Serial Total Energy Package (CASTEP).[32] The energy was calculated using PbEsol XC functional.[33] Cutoff energy and k-point grids were 630 eV and 4 × 4 × 1. As illustrated in Figure 3, the following two models were used to estimate the electrostatic potential generated at oxygen site in the fluorite-type Bi_2O_2 (or Bi_2GdO_4) slab from each sublayer. The first model (cylinder model) took account of the electrostatic interactions between the oxide anion at the center of a cylinder with a radius of R (Figure 3b) and all other atoms in the cylinder. Another model (square-prism model) considered the electrostatic interaction between the oxide anion at the center of a square-prism with a side length of A (Figure 3c) and all other atoms within $-ka/2 \le x, y \le ka/2$ (k is an odd number satisfying $ka \le A \le (k+1)a$). The central oxygen was located at (x, y) = (0, 0).

In calculating the Madelung site potential at the oxygen site, we fixed the value of R (cylinder model) or A (square-prism model) and changed the z-axis range. It is important to employ an electrically neutral domain to achieve reasonable convergence when the calculation range expands. For this reason, we have defined the charge-neutral sublayer set for $(m-1)c \le |z| < mc$ (where m = 1, 2, 3...) as U_1, U_2, U_3,..., U_m... (see Figure S4), and calculated the Madelung potential as a function of m.

Madelung site potential of Bi_4NbO_8Cl with the distortion-free model was calculated by the Fourier method incorporated in the VESTA program.[34] The radius of an ionic sphere and the reciprocal-space range were, respectively, set at 1.8 Å and 3 $Å^{-1}$ after convergence of the Madelung site potentials with respect to these two parameters were checked.

Results and Discussion

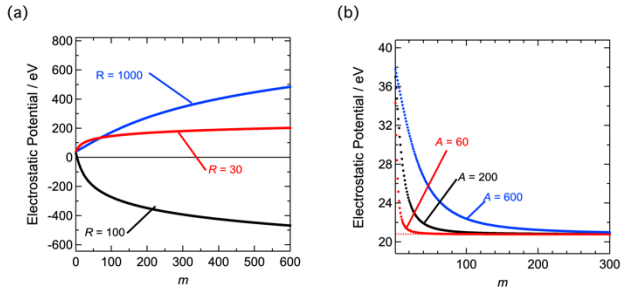

Figure 4. The *m* dependence of total electrostatic potential at the oxygen site of BiOCl calculated with (a) the cylinder model and (b) the square-prism model, for a fixed size of circle (*R* = 30 Å, 100 Å and 1000 Å) and square (*A* = 60 Å, 200 Å and 600 Å). Madelung potential obtained by Fourier method (corresponding to the infinite-size limit) is shown by the dotted red line in (b).

We first applied the two models to BiOCl and checked how the Madelung potential at the oxide anion of BL from adjacent sublayers evolves and is converged into the theoretical value when the lateral size included in the calculation increases. In the cylinder model, the electrostatic potential as a function of *m* is largely affected by *R* (Figure 4a) and the electrostatic potential did not approach the value previously obtained by Fourier method based on the calculation in reciprocal space, which is probably because the electrical neutrality is not guaranteed in this model.[15, 34] In the square-prism model, on the contrary, the electrostatic potential converged rapidly with *A* (Figure 4b). Regardless of the choice of *A*, the electrostatic potential monotonically decreased with *m* and quickly converged to the expected value of 20.8 eV (Figure 4b).

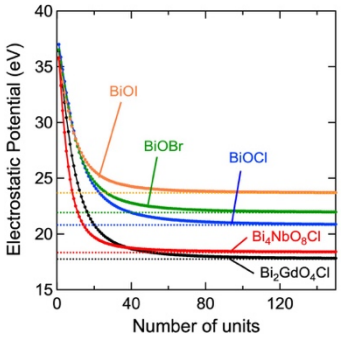

Figure 5. Total electrostatic potential created at the oxygen site (in fluorite-type layer) for BiOX, Bi_2GdO_4Cl and Bi_4NbO_8Cl, plotted with respect to the number of U_m. Madelung site potentials of the oxygen site obtained by the Fourier method (implemented in VESTA program[34]) are shown by the dotted lines. Madelung site potentials of BiOX and Bi_2GdO_4Cl are taken from the previous report,[15] while a non-distorted structure was used for Bi_4NbO_8Cl.

These results indicate that the square-prism model is more appropriate, so this model was applied to other Bi-containing oxyhalides (Figure 5). The electrostatic potential for *A* = 200 Å successfully converged to a value close to that obtained from the Fourier method: 21.9 eV for BiOBr, 23.7 eV for BiOI and 17.8 eV for Bi_2GdO_4Cl. As for Bi_4NbO_8Cl, we encountered a problem of conditional convergence[35] even for the square-prism model; Due to the orthorhombic structure involving octahedral rotations (Figure S2), it was not possible to find an appropriate charge-neutral domain. Therefore, a non-distorted tetragonal structure (*P4/mmm* space group) was constructed. The difference in lattice parameters before and after optimization of this hypothetical structure is 1.23% (Tables S1 and S3), which is within the margin of error of DFT calculation using PBEsol XC functionals. Using this hypothetical structure, we obtained the Madelung site potential of 18.3 eV by Fourier method for the oxygen site in the fluorite-type Bi_2O_2. This is similar to the values for the actual structure (O1: 18.9 eV, O2: 18.2 eV, O3: 18.3 eV, O4: 17.5 eV),[15] suggesting that the presence of octahedral tilting does not significantly influence the Madelung site potential. The electrostatic potential at the oxygen site using the non-distorted model converged well to the value obtained by the Fourier method (Figure 5).

Figure 6 shows the electrostatic potentials for BiOCl and Bi_2YO_4Cl from BL, $1NNL_u$ and $2NNL_u$ plotted as a function of *A*. Because of common units (BL: $[O_2]$, 1NNL: [Bi] and 2NNL: [Cl]), the electrostatic potentials of each sublayer are almost the same. Moreover, the Madelung potential from each sublayer exhibits a linear dependence, with the slope ratio of BL:1NNL:2NNL = 4:3:1 corresponding to the ratio of the formal charge in each sublayer: $[O_2]^{4-}$, $[Bi]^{3+}$ and $[Cl]^-$ (see Supporting Information for details).

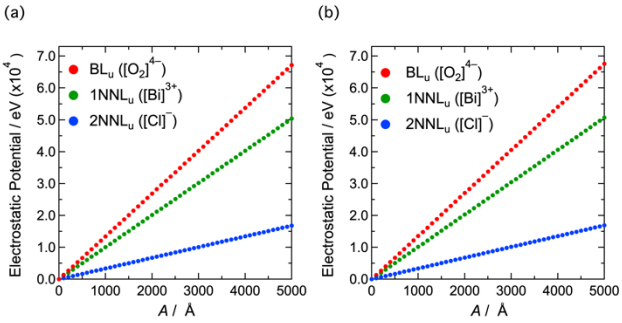

Figure 6. The *A* dependence of the absolute value of electrostatic potential from BL, $1NNL_u$ and $2NNL_u$ in (a) BiOCl and (b) Bi_2GdO_4Cl calculated using the square-prism model.

The sphere model, employed previously,[15] revealed that the Madelung site potential at the oxygen site in Bi_2O_2 slabs of Bi_4NbO_8Cl (18.2 eV on average) is smaller than that of BiOCl (20.8 eV), which was attributed to the smaller electrostatic potential generated from $2NNL_d$ in Bi_4NbO_8Cl (–20.3 eV *vs* –9.0 eV for BiOCl; Figure S3). However, when Bi_4NbO_8Cl and Bi_2GdO_4Cl are compared, the oxygen site in the latter is much more destabilized by $2NNL_d$ (–40.0 eV of Bi_2GdO_4Cl *vs* –20.3 eV of Bi_4NbO_8Cl) as shown in Figure 2. To address this reason, the electrostatic potentials from several sublayers for Bi_2GdO_4Cl

and hypothetical Bi_4NbO_8Cl were calculated using square-prism model with A = 200 Å (Figure 2). It is seen that while BL, 1NNLs and $2NNL_u$ of the two compounds generate nearly the same electrostatic potential, the electrostatic potential of Bi_2GdO_4Cl from $2NNL_d$ is almost twice as large as that of Bi_4NbO_8Cl. Although $2NNL_d$ in both compounds has an oxygen square network, their densities are different, with the formal charges of $[O_2]^{4-}$ in Bi_2GdO_4Cl and $[O]^{2-}$ in Bi_4NbO_8Cl. Importantly, this model unveils the crucial contribution from 3NNL. Since $3NNL_u$ for both compounds is composed of the $[Bi]^{3+}$ sublayer (Figure 1), little difference is seen in electrostatic potential. On the other hands, $3NNL_d$ of Bi_4NbO_8Cl consists of Nb square network ($d_{Nb\text{-}Nb}$ = 3.9 Å = a) and O square network ($d_{O\text{-}O}$ = 2.7 Å = $1/\sqrt{2}a$), while that of Bi_2GdO_4Cl consists of Bi square network ($d_{Bi\text{-}Bi}$ = 3.9 Å), giving electrostatic potentials of 662 eV and 1935 eV, respectively. These values again correlate with the formal charges of $[NbO_2]^+$ and $[Bi]^{3+}$. Accordingly, stabilization of Bi_4NbO_8Cl (*vs.* Bi_2GdO_4Cl) by $2NNL_d$ is compensated by destabilization by $3NNL_d$, which accounts for the similar values of Madelung site potential in these compounds. The present result demonstrates that 3NNLs provide a substantial impact on the Madelung potential at the oxygen site in BL, thereby affecting the valence band structures.

Let us briefly discuss the influence of halogen anions on Madelung potential by comparing the isostructural series, BiOX or Bi_2GdO_4X (X = Cl, Br, I). The Madelung site potential of BiOX increases with increasing the ionic radius of X, r_X, whereas that of Bi_2GdO_4X hardly changes (Figure S1). This results from highly anisotropic lattice expansion (Table S4); $\Delta c/\Delta a$ is 16.2 for BiOX and 13.2 for Bi_2GdO_4X, where Δa and Δc are the differences in lattice constant between X = Cl and I. The evolution of the interlayer distance is more pronounced for Bi–X and X–X (Figure S6). In particular, the X–X distance in BiOX (2NNLs and 3NNLs) remarkably changes with X. It is then likely that the predominant expansion electrostatically stabilizes the oxygen layer (BL), indicating that double halogen layer can be used to tune the Madelung site potential.

Now that we possess a tool (square-prism model) that can evaluate the impact of distant sublayer, we are ready to apply the square-prism model to other layered compounds. This model was applied to $Sr_3Sc_2Cu_2S_2O_5$ and $Sr_2ScCuSO_3$ with antifluorite Cu_2S_2 layer as shown in Figure 7a. They show exitonic luminescence properties, which can be tuned by composition and stacking pattern.[30] $Sr_3Sc_2Cu_2S_2O_5$ is also a promising p-type transparent conductor due to its high conductivity and a large band gap.[24] Madelung potential at the sulfur site (BL) for $Sr_3Sc_2Cu_2S_2O_5$ is 17.0 eV, which is smaller than 18.2 eV for $Sr_2ScCuSO_3$. As shown in Figure 7b, sublayers up to 3NNLs and $4NNL_u$ are common to the two compounds and thus give nearly the same electrostatic potential. Smaller Madelung potential of $Sr_3Sc_2Cu_2S_2O_5$ can be attributed to smaller electrostatic potential from $4NNL_d$ sublayer in $Sr_3Sc_2Cu_2S_2O_5$ composed of $[ScO_2]^-$ compared with that of $4NNL_d$ in $Sr_2ScCuSO_3$ composed of $[SrO]^0$ sublayer.

Bi_2WO_6, a visible-light responsive photocatalyst,[36] has a layer stacking similar to Bi_4NbO_8Cl with fluorite-type Bi_2O_2 and perovskite-type WO_4 layers, but halogen layer is absent (Figure 8a). The Madelung potential at the oxygen site in Bi_2O_2 layer is 14.9 eV on average, which is much smaller than that of Bi_4NbO_8Cl (18.2 eV). The L²MP analysis using a hypothetical non-distorted lattice (Figure 8b) shows that the difference arises from a smaller electrostatic potential from $[O]^{2-}$ sublayer in $2NNL_u$ (*vs.* $[Cl]^-$ sublayer in Bi_4NbO_8Cl). Thus, one expects a lower VBM for Bi_2WO_6. However, the experimentally obtained VBM of Bi_2WO_6 of 2.68 V (vs SHE at pH 2.0) is much lower than that of Bi_4NbO_8Cl of 2.27 V.[12] Such discrepancy implies that other factors, such as hybridization effect between Bi 6s orbitals and O 2p orbitals, which has been shown to be quite strong in Bi_4NbO_8Cl.[16]

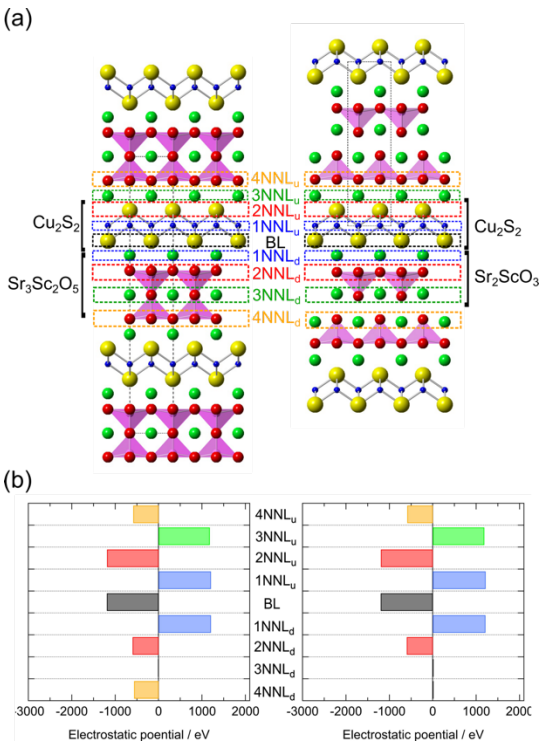

Figure 7. (a) Crystal structures of $Sr_3Sc_2Cu_2S_2O_5$ (left) and $Sr_2ScCuSO_3$ (right) with antifluorite-derived Cu_2S_2 layers. The S layer and its neighboring sublayers (*n*-th nearest-neighbor layer; *n*NNL) are indicated. Blue, yellow, green and red spheres, respectively, represent Cu, S, Sr and O atom, and ScO_5 pyramids are shown in pink. (b) Electrostatic potential at the sulfur site in the Cu_2S_2 layer from adjacent sublayers calculated using the square-prism model with A = 200 Å.

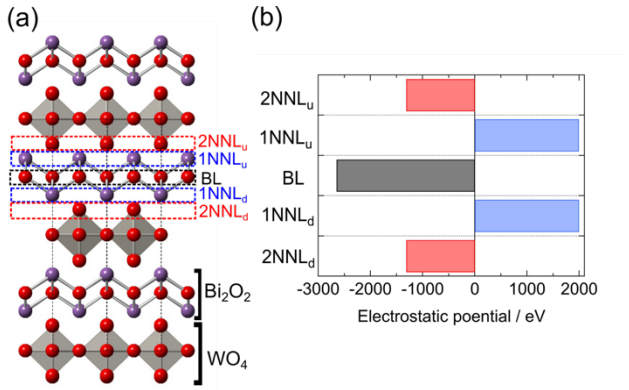

Figure 8. (a) The non-distorted structure of Bi_2WO_6. The fluorite-derived basal layer (BL) and its neighboring sublayers (*n*-th nearest-neighbor layer; *n*NNL) are indicated. Purple and red spheres represent Bi and O atom, respectively. (b) Electrostatic potential at the oxygen site of Bi_2WO_6 in the fluorite-type (BL) layer from adjacent sublayers calculated using the square-prism model with A = 200 Å.

Conclusions

We investigate the influence of distant sublayer on Madelung site potential by developing an alternate model for L²MP analysis and applying it to Bi_2O_2-based oxyhalide photocatalysts (BiOX, Bi_2GdO_4X and Bi_4NbO_8X) and other layered materials. Among the two models examined, the square-prism model shows better convergence. A significant contribution of electrostatic potential from 3NNL explains nearly the same Madelung site potential between Bi_2GdO_4Cl and Bi_4NbO_8Cl. In addition, a strong X dependence of the Madelung site potential is observed in BiOX. The L²MP analysis for Bi_2WO_6, $Sr_3Sc_2Cu_2S_2O_5$ and $Sr_2ScCu_5O_3$ further revealed a distant layer contribution to the Madelung site potential. Given the enormous variations of composition and layer stacking sequence in layered oxyhalides and more generally mixed-anion compounds,[37] L²MP analysis offers a large potential for a prediction and tuning of desired valence band structures for photocatalytic applications and other functions, possibly with an aid of machine learning approach.

Conflicts of interest

The authors declare no competing financial interest.

Acknowledgements

This work was supported by the Grant-in-Aid for Scientific Research on Innovative Areas “Mixed Anion” project (JP16H06439, JP16H06440, and JP16H06441) from MEXT and CREST (JPMJCR1421).

References

1. P. A. Cox, *The electronic structure and chemistry of solids.*, Oxford University Press, Oxford, United Kingdom, 1986.
2. A. H. Kahn and A. J. Leyendecker, *Phys. Rev.*, 1964, **135**, A1321-A1325.
3. J. D. Levine and S. Freeman, *Phys. Rev. B*, 1970, **2**, 3255-3272.
4. J. B. Torrance and R. M. Metzger, *Phys. Rev. Lett.*, 1989, **63**, 1515-1518.
5. Y. Ohta, T. Tohyama and S. Maekawa, *Phys. Rev. Lett.*, 1991, **66**, 1228-1231.
6. Y. Ohta, T. Tohyama and S. Maekawa, *Phys. Rev. B*, 1991, **43**, 2968-2982.
7. I. Hase and T. Yanagisawa, *Phys. Rev. B*, 2007, **76**, 174103.
8. A. Walsh, *Appl. Phys. Lett.*, 2011, **98**, 261910.
9. D. O. Scanlon, C. W. Dunnill, J. Buckeridge, S. A. Shevlin, A. J. Logsdail, S. M. Woodley, C. R. Catlow, M. J. Powell, R. G. Palgrave, I. P. Parkin, G. W. Watson, T. W. Keal, P. Sherwood, A. Walsh and A. A. Sokol, *Nat. Mater.*, 2013, **12**, 798-801.
10. J. Buckeridge, K. T. Butler, C. R. A. Catlow, A. J. Logsdail, D. O. Scanlon, S. A. Shevlin, S. M. Woodley, A. A. Sokol and A. Walsh, *Chem. Mater.*, 2015, **27**, 3844-3851.
11. H. Fujito, H. Kunioku, D. Kato, H. Suzuki, M. Higashi, H. Kageyama and R. Abe, *J. Am. Chem. Soc.*, 2016, **138**, 2082-2085.
12. H. Kunioku, M. Higashi, C. Tassel, D. Kato, O. Tomita, H. Kageyama and R. Abe, *Chem. Lett.*, 2017, **46**, 583-586.
13. H. Suzuki, H. Kunioku, M. Higashi, O. Tomita, D. Kato, H. Kageyama and R. Abe, *Chem. Mater.*, 2018, **30**, 5862-5869.
14. A. Nakada, A. Saeki, M. Higashi, H. Kageyama and R. Abe, *J. Mater. Chem. A*, 2018, **6**, 10909-10917.
15. D. Kato, K. Hongo, R. Maezono, M. Higashi, H. Kunioku, M. Yabuuchi, H. Suzuki, H. Okajima, C. Zhong, K. Nakano, R. Abe and H. Kageyama, *J. Am. Chem. Soc.*, 2017, **139**, 18725-18731.
16. H. Kunioku, M. Higashi, O. Tomita, M. Yabuuchi, D. Kato, H. Fujito, H. Kageyama and R. Abe, *J. Mater. Chem. A*, 2018, **6**, 3100-3107.
17. D. O. Charkin, *Russ. J. Inorg. Chem.*, 2008, **53**, 1977-1996.
18. Y. Tokura and T. Arima, *Jpn J Appl Phys 1*, 1990, **29**, 2388-2402.
19. Y. Kamihara, T. Watanabe, M. Hirano and H. Hosono, *J. Am. Chem. Soc.*, 2008, **130**, 3296-3297.
20. K. Tanabe and H. Hosono, *Jpn. J. Appl. Phys.*, 2012, **51**, 010005.
21. Y. Mizuguchi, *J. Phys. Soc. Jpn.*, 2019, **88**, 041001.
22. J. B. Goodenough and K. S. Park, *J. Am. Chem. Soc.*, 2013, **135**, 1167-1176.
23. K. Ueda, S. Inoue, S. Hirose, H. Kawazoe and H. Hosono, *Appl. Phys. Lett.*, 2000, **77**, 2701-2703.
24. M. L. Liu, L. B. Wu, F. Q. Huang, L. D. Chen and I. W. Chen, *J. Appl. Phys.*, 2007, **102**, 116108.
25. A. M. Kusainova, S. Y. Stefanovich, V. A. Dolgikh, A. V. Mosunov, C. H. Hervoches and P. Lightfoot, *J. Mater. Chem.*, 2001, **11**, 1141-1145.
26. M. Schmidt, H. Oppermann, C. Hennig, R. W. Henn, E. Gmelin, N. Soger and M. Binnewies, *Z. Anorg. Allg. Chem.*, 2000, **626**, 125-135.
27. K. G. Keramidas, G. P. Voutsas and P. I. Rentzeperis, *Z. Kristallogr. Cryst. Mater.*, 1993, **205**, 35-40.
28. J. Ketterer and V. Kramer, *Acta Crystallogr. C*, 1986, **42**, 1098-1099.
29. K. Otzschi, H. Ogino, J. Shimoyama and K. Kishio, *J. Low Temp. Phys.*, 1999, **117**, 729-733.
30. H. Ogino, J. Shimoyama, K. Kishio, Y. Katsura, M. Tsuboi, K. Yamanoi, M. Cadatal-Raduban, T. Nakazato, T. Shimizu and N. Sarukura, *Appl. Phys. Lett.*, 2012, **101**, 191901.
31. H. Okudera, Y. Sakai, K. Yamagata and H. Takeda, *Acta Cryst.*, 2018, **B74**, 295-303.

32. S. J. Clark, M. D. Segall, C. J. Pickard, P. J. Hasnip, M. J. Probert, K. Refson and M. C. Payne, *Z. Kristallogr. Cryst. Mater.*, 2005, **220**, 567-570.
33. J. Perdew, A. Ruzsinszky, G. Csonka, O. Vydrov, G. Scuseria, L. Constantin, X. Zhou and K. Burke, *Phys. Rev. Lett.*, 2008, **100**, 136406.
34. K. Momma and F. Izumi, *J. Appl. Crystallogr.*, 2011, **44**, 1272-1276.
35. H. M. Evjen, *Phys. Rev.*, 1932, **39**, 675-687.
36. A. Kudo and S. Hijii, *Chem. Lett.*, 1999, **28**, 1103-1104.
37. H. Kageyama, K. Hayashi, K. Maeda, J. P. Attfield, Z. Hiroi, J. M. Rondinelli and K. R. Poeppelmeier, *Nat. Commun.*, 2018, **9**, 772.

The table of content graphics

Extended layer-by-layer Madelung analysis was developed and applied to various layered materials to revealed the contribution of distant layer to Madelung site potential.